Materials Science & Engineering A 738 (2018) 90–97

Contents lists available at ScienceDirect

Materials Science & Engineering A

journal homepage: www.elsevier.com/locate/msea

Anisotropic multiaxial plasticity model for laser powder bed fusion additively manufactured Ti-6Al-4V

Alexander E. Wilson-Heid[a], Shipin Qin[a], Allison M. Beese[a,b,*]

[a] Department of Materials Science and Engineering, Pennsylvania State University, University Park, PA 16802, United States
[b] Department of Mechanical Engineering, Pennsylvania State University, University Park, PA 16802, United States

ARTICLE INFO

Keywords:
Stress state
Plasticity
Ti-6Al-4V
Additive manufacturing
Powder bed fusion

ABSTRACT

The multiaxial yield and plastic flow behavior of Ti-6Al-4V manufactured in two orientations via laser powder bed fusion (L-PBF) additive manufacturing was investigated. The mechanical properties of L-PBF Ti-6Al-4V were evaluated under uniaxial tension, plane strain tension, pure shear, and combined tension/shear loading. The mechanical behavior was found to be stress state dependent and slightly anisotropic. A plasticity model, consisting of a Hill 1948 anisotropic yield criterion, associated flow rule, and an isotropic hardening law was calibrated and used to describe the yield and plasticity behavior of this material. Validation of the plasticity model under multiaxial stress states demonstrated that the model was able to predict the stress state dependent anisotropic plasticity behavior of this material.

1. Introduction

Additive manufacturing (AM) is the process of building a 3-dimensional (3D) component layer-by-layer [1]. In laser powder bed fusion (L-PBF) AM, a thin layer of metal powder is spread on top of a baseplate, and a laser scans the 2D layer pattern, melting the powder and allowing it to fuse to the material below. This process is repeated as the baseplate is lowered, powder is spread on the previous layer, and a new layer is scanned until the 3D component is fabricated. The most commonly adjusted processing parameters in L-PBF include laser power, scanning speed, layer height, and scan pattern. Altering these parameters results in varying morphology and size of both grains and defects in a fabricated component [2].

The microstructures in AM are different from traditionally processed counterparts due the rapid solidification and thermal cycling of the material during processing [3,4]. Material in L-PBF can undergo cooling rates of up to 10^6 K/s at the solidification front [5], and after solidification undergoes thermal cycles as material is added above or adjacent to the previously solidified material. The unique microstructures in materials made by AM influence the mechanical properties of the completed parts.

The present study focuses on Ti-6Al-4V, an α-β titanium alloy that exhibits high strength, stiffness, and corrosion resistance [6]. This alloy has been widely studied in the AM field, both because of its suitability for building complex part geometries for use in the aerospace and biomedical industries [7,8] and because of the high cost associated with traditional subtractive machining of this material [9].

The strength of Ti-6Al-4V fabricated via L-PBF has been investigated previously. In Ti-6Al-4V, both the yield and ultimate tensile strengths have been reported as greater than those values seen in traditionally manufactured material [2,10–13]. This result can be explained by the rapid cooling in AM leading to the formation of fine acicular α and α' laths in the L-PBF material, which are stronger than the lamellar α + β structure seen in as-cast and annealed versions of this alloy [14].

Additionally, the elongation to failure under uniaxial tension (UT) of Ti-6Al-4V fabricated via AM has been experimentally measured [15,16]. When compared to their traditionally manufactured counterparts, Ti-6Al-4V that has been fabricated via L-PBF has lower ductility, which can be explained by microstructural differences [12]. In the L-PBF condition, lack-of-fusion (LoF) defects between laser passes can result from non-optimal processing parameters, laser power or beam size fluctuations, or recoating errors [17,18]. The elongated, irregularly shaped LoF defects are detrimental to the ductility of the bulk material as the sharp corners in these defects act as stress concentration sites that lead to early failure [19]. Furthermore, α and α' phases, which are the primary phases in Ti-6Al-4V made by L-PBF, have limited plastic deformability compared to the β phase typically present in the conventionally processed material [20]. Together, these features result in a decrease in the macroscopic ductility of additively manufactured Ti-6Al-4V compared to conventionally processed Ti-6Al-4V.

* Corresponding author.
E-mail address: beese@matse.psu.edu (A.M. Beese).

https://doi.org/10.1016/j.msea.2018.09.077
Received 15 May 2018; Received in revised form 19 September 2018; Accepted 20 September 2018
Available online 21 September 2018
0921-5093/

The mechanical properties of additively manufactured Ti-6Al-4V have been predominantly assessed under uniaxial tension as described above. These tests provide information about mechanical behavior, including elongation, strain hardening behavior, and yield stress under uniaxial tension. However, these properties only define the mechanical behavior under the single stress state of uniaxial tension, which is not sufficient to completely describe how additively manufactured components will behave under realistic loading, which will subject the material to multiaxial stress states. An investigation into materials under multiaxial stress states is critical because the plasticity and fracture behavior of a ductile metal may be stress state dependent [21–24]. Since a well-defined plasticity model is required for quantitatively investigating fracture, it is critical to first experimentally determine and model the plasticity behavior of the material under different stress states, even if the plasticity behavior of the material is stress state independent, before fracture properties can be assessed. In the current work, the stress state and orientation dependent plasticity behavior was investigated through multiaxial loading tests.

The mechanical behavior of conventionally processed Ti-6Al-4V has been studied under multiaxial loading states, with an emphasis on studying the effects of temperature and strain rate on properties, which are relevant to the applications and forming processes of conventional Ti-6Al-4V. Studies on conventionally processed Ti-6Al-4V have found that the mechanical properties of this material are often anisotropic and stress state dependent. Tuninetti and co-workers found that a Ti-6Al-4V ingot exhibited tension/compression asymmetry, anisotropic yield behavior, and anisotropic strain hardening [25]. An orthotropic yield criterion for hexagonal close packed metals, developed by Cazacu and co-workers [26], was used to describe the initial yield behavior. Hammer and co-workers, found that the mechanical behavior of aerospace grade Ti-6Al-4V plate was dependent on loading condition [27] and was anisotropic [28].

A plasticity and fracture model for wire-based directed energy deposition additively manufactured Ti-6Al-4V was proposed by Gorji and co-workers using analogies to crystal plasticity finite element analysis [29]. The microstructure of this material consisted of large prior-β grains that were several millimeters wide and several centimeters in length, which contained α needles. Their model incorporates statistical variations in the properties of single prior-β grains, based on tension and shear tests, and determines macroscopic mechanical properties by incorporating a random sampling of these statistical properties to account for many prior-β grains within a material.

In the present paper, we experimentally characterized and computationally modeled the plasticity behavior of L-PBF fabricated Ti-6Al-4V, considering both uniaxial and multiaxial stress states. An accurate plasticity model that predicts the mechanical response of complex-shaped additively manufactured Ti-6Al-4V components under loading is required for the adoption of these components in structural applications. Here, L-PBF Ti-6Al-4V was studied under uniaxial tension, pure shear (PS), plane strain tension (PST), and combined tension/shear loading conditions, and the initial yield and strain hardening behavior were measured. A plasticity model that captures the anisotropic and stress state dependent mechanical behavior of this material under multiaxial loading was calibrated based on experimental results and validated using finite element simulations.

2. Experimental procedures

2.1. Sample fabrication

Ti-6Al-4V walls were fabricated using L-PBF AM (EOSINT M280). The pre-alloyed Ti-6Al-4V powder was manufactured by EOS Gmbh via argon gas atomization and had a chemical composition in accordance with ASTM F1472 and F2924 [30,31]. Standard EOS processing parameters for Ti-6Al-4V with a 60 μm layer thickness were used, resulting in a linear heat input of 0.27 J/mm and a volumetric heat input of 32.4 J/mm^3 [1].

Table 1
As-built wall sample dimensions and number of samples tested in each orientation.

Sample description	As-built wall dimensions: width × thickness × height (mm)	Number of Samples
UT: BD	12 × 4 × 65.5	2
UT: ⊥ BD	65.5 × 4 × 12	2
Multiaxial Loading: BD	70 × 3.5 × 27.4	8
Multiaxial Loading: ⊥ BD	27.4 × 3.5 × 70	8

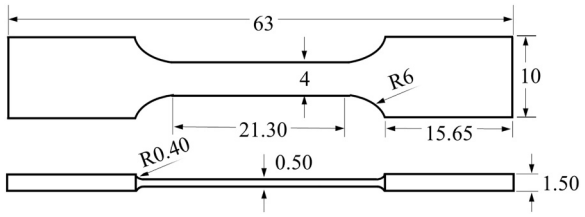

Fig. 1. Geometry of tensile samples extracted from as-built walls. Dimensions are in mm.

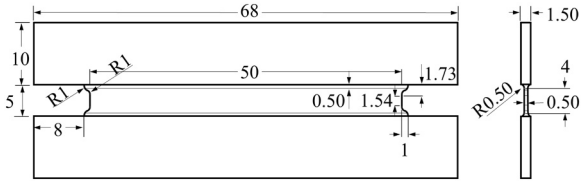

Fig. 2. Geometry of multiaxial loading samples extracted from as-built walls. Dimensions are in mm. Adapted from [33].

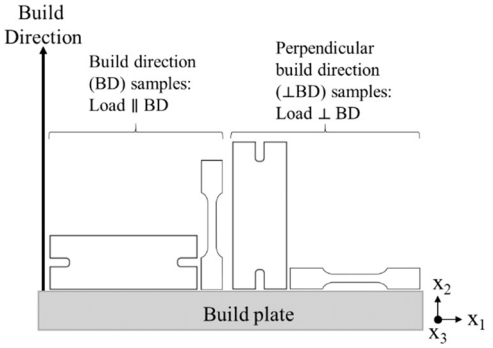

Fig. 3. Schematic of sample orientation nomenclature with respect to vertical build direction (BD) where the outlines correspond to sample geometries in Figs. 1 and 2. All of the specimens were extracted from the x_1-x_2 plane.

All specimens used for mechanical testing were extracted from the thin walls, which had the dimensions given in Table 1. Prior to machining the walls off of the build plate, or machining test specimens out of the walls, the entire build plate was subjected to a standard stress relief heat treatment of 650 °C for 3 h in an argon environment. Uniaxial tension, in accordance with ASTM E8 [32], (Fig. 1) and multiaxial loading (Fig. 2) specimens were extracted from the walls in the build direction (BD) and perpendicular to the build direction (⊥ BD) using wire electrical discharge machining. The gauge thickness of both uniaxial tension and multiaxial loading specimens was 0.5 mm to remove any potential size effects in the mechanical property measurements. A schematic of the orientation nomenclature is given in Fig. 3. Note that all the specimens were extracted from the x_1-x_2 plane. All specimens are under plane stress

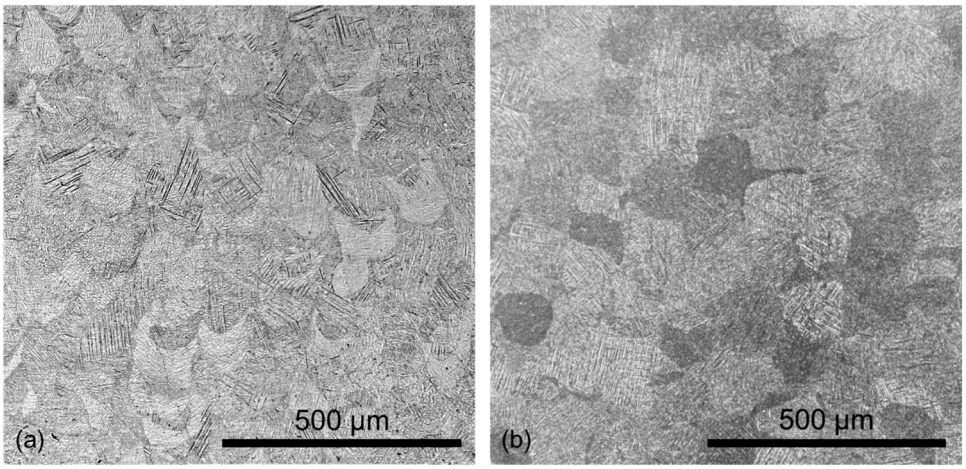

Fig. 4. Micrographs of L-PBF Ti-6Al-4V in the (a) x_1-x_2 plane and (b) x_1-x_3 plane. The melt pool is shown to have influence on the morphology of the prior-β grains, which are filled with acicular α or α′ laths. The scale bar is equivalent to the thickness of the gauge regions of mechanical test specimens shown in Figs. 1 and 2.

in the x_1-x_2 plane (zero stress along the x_3 direction due to the thin thickness along this direction). In addition, the width to height aspect ratio of the gauge region in the multiaxial loading specimen geometry also results in a plane strain condition, with zero strain along the horizontal direction of the specimen (x_1 direction for BD samples and x_2 direction for ⊥ BD samples) [33].

Representative micrographs, in two perpendicular planes, of the L-PBF Ti-6Al-4V in this study are given in Fig. 4. For microstructural analysis, the samples were prepared using standard metallurgical procedures with a final polish using 0.05 μm colloidal silica and etched using Kroll's reagent (2 vol% hydrofluoric acid and 3 vol% nitric acid in distilled water). The images of the microstructure were taken using a digital microscope (Keyence VHX- 2000).

2.2. Mechanical testing

An electromechanical load frame (MTS Criterion Model 43) with a 10 kN load cell (MTS model LPS-104A) was used to perform uniaxial tension tests. The tests were performed under displacement control with an applied strain rate on the order of 10^{-4} s^{-1}. Multiaxial loading tests were performed on a custom-built dual-actuator hydraulic loading machine (MTS Inc., see Fig. 5). The dual-actuator test frame is equipped with two 100 kN load cells in the vertical direction (y) and one 50 kN load cell in the horizontal direction (x). To access plane strain tension, the samples were loaded at 0.1 mm/min in the vertical direction, with the horizontal actuator fixed. To access pure shear, the samples were loaded at 0.8 mm/min in the horizontal direction, with the vertical force set to zero. For combined tension/shear tests, the ratio of the applied vertical force, F_y, to horizontal force, F_x, is described by the loading angle, β, where:

$$\beta = \tan\left(\frac{F_y}{F_x}\right) \quad (1)$$

Combined tension/shear loading tests were performed under force control. For tests where β = 30°, values of F_y = 0.866 kN/min and F_x = 1.5 kN/min were used, and the opposite loading rates were used to access the β = 60° condition.

For all tests, the surface deformation fields were measured using digital image correlation (DIC), a non-contact strain measurement technique (Vic2D software, Correlated Solutions). For the analysis, gauge regions of the samples were painted with a flat white basecoat, and a random black speckled pattern was painted on top of the basecoat. A digital camera (Point Grey GRAS-50S5M-C) was used to take images of the samples at a rate of 1 Hz during loading until fracture. The 2D surface deformation fields in the gauge region of each sample were computed from the digital images using a cubic B-spline interpolation algorithm. DIC parameters used were a subset size of 21 pixels, a step size of 5 pixels, and a strain window of 15 pixels for an overall virtual strain gauge of 71 pixels [34]. The axial strain in the uniaxial tension samples was computed using an 18 mm-long vertical virtual extensometer. For the multiaxial loading tests, the surface strains were evaluated at the center of the gage region, and axial and shear strains were computed with a 3 mm vertical virtual extensometer.

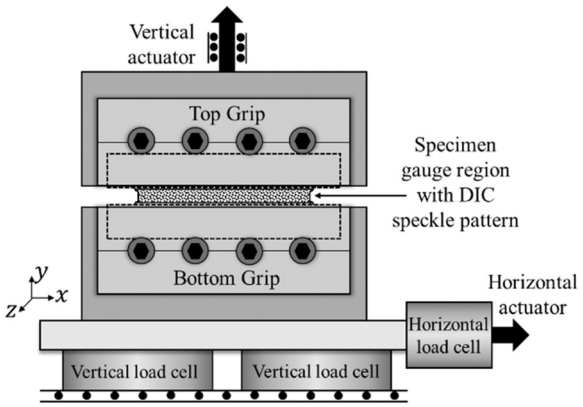

Fig. 5. Schematic of the dual-actuator load frame used to perform multiaxial tests (pure shear, plane strain tension, β = 30°, and β = 60°) using specimens shown in Fig. 2.

3. Results and discussion

3.1. Uniaxial tension results

Fig. 6 shows the engineering stress-strain curves for the uniaxial tension tests. The elastic modulus of the material in both orientations was 103.2 ± 1.3 GPa. The yield strength (0.2% offset) and ultimate tensile strength of the material were similar in the BD and ⊥ BD directions. Specifically, the average yield strengths were measured to be 1060 MPa in the BD and 1031 MPa in the ⊥ BD, while the average ultimate tensile strengths were measured to be 1113 MPa in the BD and 1105 MPa in the ⊥ BD. However, the elongation to failure was orientation dependent, as the average ductility in the BD direction was 9.3%, compared to 6.7% in the ⊥ BD.

In order to propose a conservative plasticity model for this material, considering the fact that scatter of mechanical properties is often

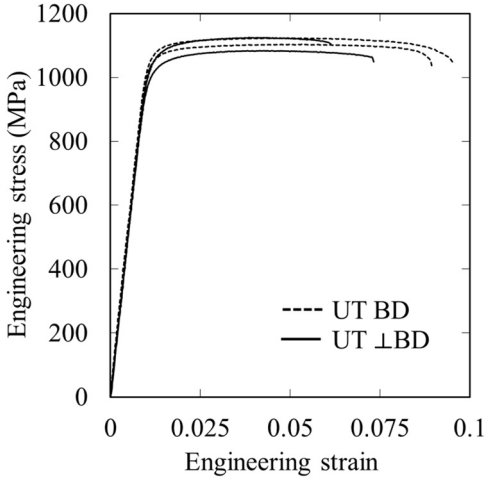

Fig. 6. Engineering stress-strain curves for uniaxial tension in the build direction and the perpendicular build direction.

observed in materials made by AM [35], the lower bound of the uniaxial tension results were adopted for model development.

3.2. Hardening behavior

In the present study, the evolution of the yield strength can be described by the Swift law before necking and a linear extrapolation after necking as:

$$\Delta \sigma_y = \begin{cases} nA(\varepsilon_0 + \bar{\varepsilon}^p)^{n-1}\,\Delta\bar{\varepsilon}^p & \bar{\varepsilon}^p \le 0.038 \\ K\Delta\bar{\varepsilon}^p & \bar{\varepsilon}^p > 0.038 \end{cases} \quad (2)$$

where σ_y is the flow stress at an equivalent plastic strain of $\bar{\varepsilon}_p$, and A, ε_0, n, and K are material constants. To determine the slope of the linear extrapolation portion of the hardening curve, an inverse method was used in which the criterion for acceptance was to reproduce the experimentally measured engineering stress-strain behavior under uniaxial tension. The experimental data used to fit the hardening behavior, compared with calibrated Eq. (2), for both directions, are given in Figs. 7a and 7b, while the calibrated parameters are given in Table 2. The simulated engineering stress-strain curves used for validation of these parameters are compared with experimentally measured values in Fig. 7c.

3.3. Multiaxial loading results

Multiaxial loading tests were performed to study the mechanical behavior of the material as a function of stress state and material orientation. Fig. 8 shows the anisotropy of the plasticity behavior under five loading conditions, while Fig. 9 highlights the stress state-dependency of the plasticity behavior. As shown in Fig. 8, in all stress states studied, BD samples had higher yield strength (1017 ± 27 MPa) than their ⊥ BD counterparts (961 ± 52 MPa). Under multiaxial loading, the L-PBF Ti-6Al-4V exhibited very low ductility, with none of the samples exceeding 5.5% equivalent plastic strain before failure. The plane strain tension and β = 60° samples all failed at or below 1.0% equivalent plastic strain.

Fig. 9 shows that in each direction, the von Mises equivalent stress-strain curves depend on stress state. Therefore, the material behavior is anisotropic and stress state dependent, and the initial yield behavior and subsequent flow behavior cannot be captured using an isotropic von Mises, or J2 plasticity, framework.

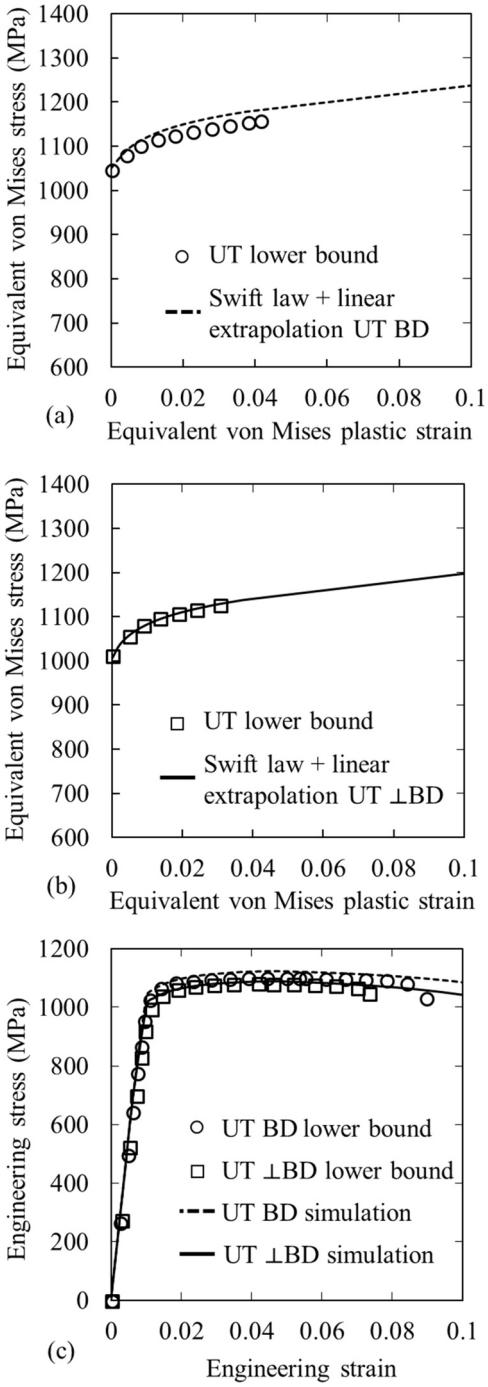

Fig. 7. Lower bound von Mises equivalent stress-plastic strain curves under uniaxial tension in the (a) build direction and (b) perpendicular build direction for L-PBF Ti-6Al-4V along with a Swift law fit prior to necking, and a linear extrapolation after necking. (c) Engineering stress-strain curves for uniaxial tension from experiments (symbols) and simulations based on the inputs in (a) and (b) (lines).

Table 2
Strain hardening parameters determined through experimental fitting of lower bound uniaxial tension tests in each orientation.

	A (MPa)	n	ε_0	K (MPa)
BD	1349	0.042	0.002	950
⊥ BD	1303	0.042	0.002	950

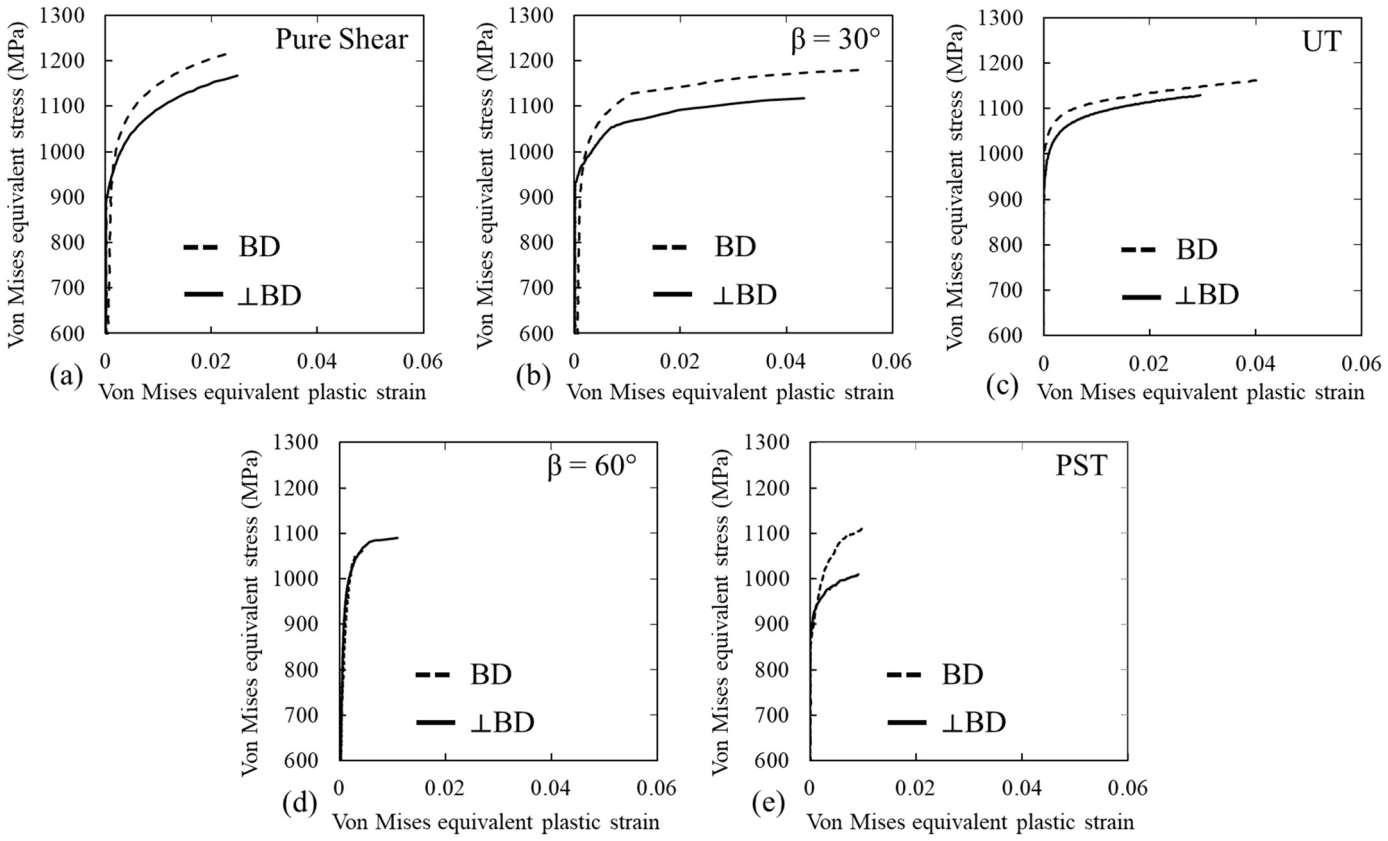

Fig. 8. Von Mises equivalent stress-plastic strain curves for (a) pure shear, (b) combined loading with β = 30°, (c) uniaxial tension, (d) combined loading with β = 60°, and (e) plane strain tension, in two directions. In all cases except for combined loading with β = 60°, the mechanical behavior showed notable anisotropy.

4. Modeling

4.1. Plasticity modeling

A plasticity framework using the Hill 1948 anisotropic yield function (Hill48) was adopted to describe the multiaxial plasticity behavior of the current material [36]. The yield function is given as:

$$f = \sigma_{\text{Hill48}} - \sigma_y = 0 \tag{3}$$

where σ_y is the yield stress, and the equivalent Hill48 stress, σ_{Hill48}, under the plane stress condition is defined as:

$$\sigma_{\text{Hill48}} = \sqrt{(G+H)\sigma_{11}^2 - 2H\sigma_{11}\sigma_{22} + (F+H)\sigma_{22}^2 + 2N\tau^2} \tag{4}$$

where G, H, F, and N are constants that describe the material's anisotropy, σ_{11} and σ_{22} are the normal stresses along x_1 and x_2 directions, respectively, as shown in Fig. 3, and τ is the shear stress component. Assuming an associated flow rule, the plastic strain increment can be calculated as:

$$\dot{\varepsilon}_{ij}^{p} = \dot{\gamma}\frac{\partial \sigma_{\text{Hill48}}}{\partial \sigma_{ij}} \tag{5}$$

where $\dot{\gamma}$ is the plastic multiplier.

In the current work, the specimens were built in two orientations, BD (y-loading direction parallel to the build direction) and ⊥ BD (y-loading direction perpendicular to the build direction). The multiaxial loading specimens were under plane strain, with zero strain along the x-

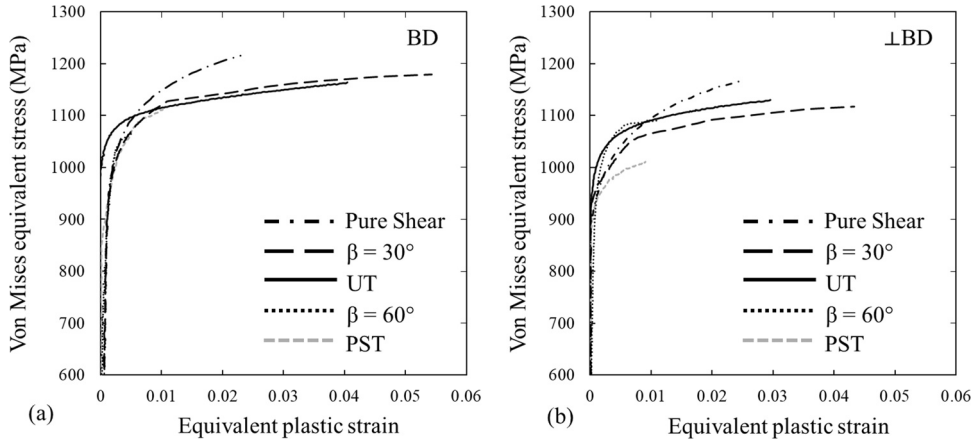

Fig. 9. Von Mises equivalent stress versus equivalent plastic strain for all stress states evaluated in both the (a) build direction and (b) perpendicular BD directions, indicating that the yield and strain hardening behavior of the material is stress state dependent.

direction in machine coordinates (see Fig. 5), along the majority of the gauge region. The x-direction was parallel to the x_1 direction for BD specimens and parallel to the x_2 direction for ⊥ BD specimens, as shown in Fig. 3. As a result, $\varepsilon_{11} \approx 0$ for BD and $\varepsilon_{22} \approx 0$ for ⊥ BD specimens. For plastic deformation, if $\varepsilon_{22}^{p} \approx 0$, the associated flow rule is given as:

$$\dot{\varepsilon}_{22}^{p} = \dot{\gamma}\frac{\partial \sigma_{\text{Hill48}}}{\partial \sigma_{22}} = \dot{\gamma}\frac{2(F+H)\sigma_{22} - 2H\sigma_{11}}{2\sigma_{\text{Hill48}}} = 0, \tag{6}$$

which gives:

$$\sigma_{22} = \frac{H}{F+H}\sigma_{11} \tag{7}$$

Correspondingly, the plane strain condition for the BD specimens gives:

$$\sigma_{11} = \frac{H}{G+H}\sigma_{22} \tag{8}$$

However, if the plastic strain is very small, as was the case in this study, then $\varepsilon_{22}^{e} \approx \varepsilon_{22} = 0$ for ⊥ BD specimens, giving:

$$\sigma_{22} = \nu\sigma_{11}, \tag{9}$$

where ν is the Poisson ratio ($\sigma_{33} = 0$ due to out-of-plane plane stress condition). Similarly, for BD specimens, $\varepsilon_{11}^{e} \approx \varepsilon_{11} = 0$ and:

$$\sigma_{11} = \nu\sigma_{22}. \tag{10}$$

Given the low level of plastic strain in the present study, Eqs. (9) and (10) were used to compute the stress along the x-direction in the multiaxial loading tests.

4.2. Model calibration

The Hill48 yield surface and subsequent hardening law were calibrated using the lower bound uniaxial tension data. The sum G + H was assumed to be 1, and F + H was determined based on the yield strength ratio under uniaxial tension along the two orientations, which can be derived from Eq. (4) as:

$$\frac{G+H}{F+H} = \left(\frac{\sigma_{y,22}}{\sigma_{y,11}}\right)^2 \tag{11}$$

The values of H and N were determined using the experimental data from pure shear and $\beta = 60^{\circ}$ tests along both orientations.

The calibrated model parameters are given in Table 3 and the calibrated Hill48 anisotropic yield surface for the L-PBF Ti-6Al-4V in this study is given in Fig. 10. The calibrated yield surface captures the multiaxial experimental data well. It is noted that the adopted Hill48 parameters are close to the values for the isotropic von Mises criterion (G + H = 1, F + H = 1, N = 1.5, and H = 0.5). Therefore, the material exhibits a clear, but limited amount of anisotropy.

4.3. Finite element simulations

To calibrate and validate the continuum plasticity model, the model was implemented in commercial finite element analysis (FEA) software ABAQUS [37]. Comparing FEA simulated mechanical behavior with experimental results allows for calibration of model parameters and subsequent validation of the calibrated model in all stress states studied.

Simulations of the uniaxial tension experiments were performed using a model of 1/8th of the tensile specimen geometry, taking advantage of symmetry, and the geometry was discretized using 18,592 C3D8 elements. Symmetry boundary conditions were adopted along all three cut planes. A uniform vertical displacement was prescribed to the grip region.

Table 3
Calibrated Hill48 yield surface model parameters.

F	G	H	N
0.4	0.47	0.53	1.45

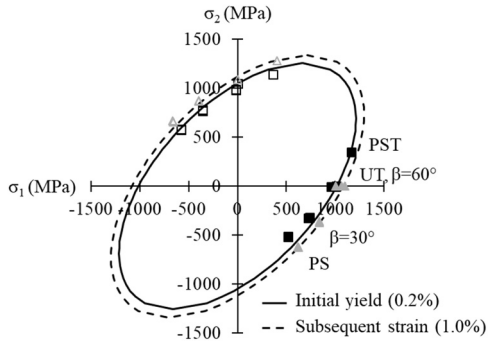

Fig. 10. Anisotropic Hill48 2D yield surface (for plane stress) at initial yield (0.2% strain) and subsequent strain (1.0%) of L-PBF Ti-6Al-4V. The fitted yield surfaces are shown as lines, while experimental data are shown as symbols. Solid symbols represent perpendicular build direction samples, while open symbols represent build direction samples.

Additionally, finite element models were created to simulate the multiaxial mechanical tests studied. To simulate the multiaxial loading tests, 2D single element models measuring 1 mm by 1 mm were used. Due to the through thickness plane stress condition of the multiaxial loading specimens, a four node 2D plane stress element (CPS4) was used. For all multiaxial loading cases, the lower boundary was fixed in the vertical direction, and the lengths of the bottom and top surfaces of the element were fixed. To evaluate plane strain tension, a uniform vertical displacement was applied to the two upper nodes, with the left and right edges constrained in the horizontal direction. For pure shear, a horizontal displacement was prescribed to the top nodes, and the vertical force was set to zero. For combined loading, concentrated forces in both the horizontal and vertical directions were applied to the top nodes such that the two desired loading angles were fulfilled.

4.4. Model validation

As model calibration was performed using data from uniaxial tension, pure shear, and combined tension/shear loading tests with $\beta = 60^{\circ}$, the model was validated using data from plane strain tension and combined tension/shear loading tests with $\beta = 30^{\circ}$. In both the BD and ⊥ BD orientations, the experimental results lie on or very close to the calibrated yield surface. The developed model is able to predict the evolving flow stress behavior of the material in both build orientations and in all stress states evaluated as shown in Fig. 11. The maximum percent difference in normal engineering stress for a given strain between those predicted using the plasticity model and those experimentally measured is 4.1% for BD and 3.1% for ⊥ BD specimens across all stress states evaluated. The maximum percent difference in engineering shear stress between plasticity simulations and experiments at a given strain is 4.6% for BD and 6.0% for ⊥ BD specimens.

Therefore, the proposed plasticity model captures and predicts the anisotropy and stress state dependence of the plasticity behavior of L-PBF Ti-6Al-4V. Note that the calibrated material parameters hold for this particular L-PBF Ti-6Al-4V material, with the parameters used. This means that the approach for gathering the experimental data, and calibrating and validating the model can be applied to other additively manufactured materials, but the parameters need to be calibrated for the particular material being studied. For example, the model presented here applies to the nearly equiaxed grain structure in this L-PBF Ti-6Al-4V; however, it is anticipated that the anisotropy would be increased in a Ti-6Al-4V material with columnar prior-β grains such as in [15,38].

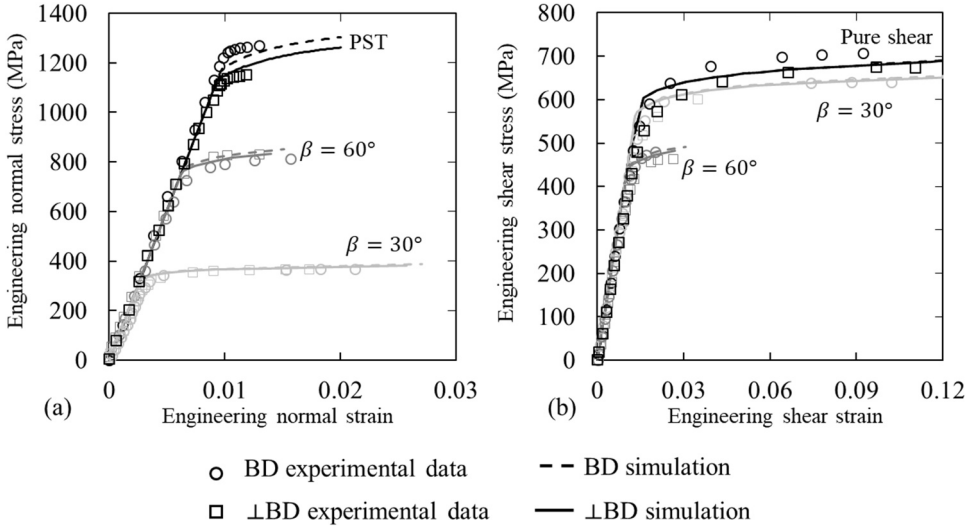

Fig. 11. (a) Normal and (b) shear engineering stress-strain curves for the four multiaxial loading conditions, showing the comparison between experimental data (symbols) and the simulation results (lines).

5. Summary and conclusions

The current work studied the multiaxial yield and plastic flow behavior of L-PBF Ti-6Al-4V. Using experimental results that are novel to the AM community, a calibrated and validated anisotropic and stress state dependent plasticity model was proposed. The main takeaways from this study include:

- L-PBF Ti-6Al-4V was found to be anisotropic under all stress states evaluated (uniaxial tension, plane strain tension, pure shear, and combined tension/shear loading).
- The yield and flow behavior of L-PBF Ti-6AL-4V was found to be stress state dependent.
- The calibrated plasticity model, consisting of an anisotropic Hill48 yield criterion, an associated flow rule, and an isotropic strain hardening law, captures and predicts the anisotropic and stress state dependent initial yield and subsequent flow behavior of L-PBF Ti-6Al-4V. The ability to describe and predict the multiaxial deformation behavior of additively manufactured Ti-6Al-4V is required for its safe adoption in structural applications.

Acknowledgments

The financial support provided by the National Science Foundation through award numbers CMMI-1402978 and CMMI-1652575 is gratefully acknowledged. Any opinions, findings, and conclusions or recommendations expressed in this material are those of the authors and do not necessarily reflect the views of the National Science Foundation. The samples were fabricated at Penn State's Center for Innovative Materials Processing through Direct Digital Deposition (CIMP-3D).

Data availability

All relevant data are available from the authors.

References

[1] T. DebRoy, H.L. Wei, J.S. Zuback, T. Mukherjee, J.W. Elmer, J.O. Milewski, A.M. Beese, A. Wilson-Heid, A. De, W. Zhang, Additive manufacturing of metallic components – process, structure and properties, Prog. Mater. Sci. 92 (2018) 112–224, https://doi.org/10.1016/j.pmatsci.2017.10.001.

[2] S. Cao, Z. Chen, C.V.S. Lim, K. Yang, Q. Jia, T. Jarvis, D. Tomus, X. Wu, Defect, microstructure, and mechanical property of Ti-6Al-4V alloy fabricated by high-power selective laser melting, JOM (2017) 1–9, https://doi.org/10.1007/s11837-017-2581-6.

[3] W.J. Sames, F.A. List, S. Pannala, R.R. Dehoff, S.S. Babu, The metallurgy and processing science of metal additive manufacturing, Int. Mater. Rev. 61 (2016) 315–360, https://doi.org/10.1080/09506608.2015.1116649.

[4] D.D. Gu, W. Meiners, K. Wissenbach, R. Poprawe, Laser additive manufacturing of metallic components: materials, processes and mechanisms, Int. Mater. Rev. 57 (2012) 133–164, https://doi.org/10.1179/1743280411Y.0000000014.

[5] U. Scipioni Bertoli, G. Guss, S. Wu, M.J. Matthews, J.M. Schoenung, In-situ characterization of laser-powder interaction and cooling rates through high-speed imaging of powder bed fusion additive manufacturing, Mater. Des. 135 (2017) 385–396, https://doi.org/10.1016/j.matdes.2017.09.044.

[6] M. Donachie Jr., Titanium: A Technical Guide, 2nd ed., ASM International, Materials Park, OH, 2000.

[7] L.E. Murr, S.A. Quinones, S.M. Gaytan, M.I. Lopez, A. Rodela, E.Y. Martinez, D.H. Hernandez, E. Martinez, F. Medina, R.B. Wicker, Microstructure and mechanical behavior of Ti-6Al-4V produced by rapid-layer manufacturing, for biomedical applications, J. Mech. Behav. Biomed. Mater. 2 (2009) 20–32, https://doi.org/10.1016/j.jmbbm.2008.05.004.

[8] M. Brandt, S.J. Sun, M. Leary, S. Feih, J. Elambasseril, Q.C. Liu, High-value SLM aerospace components: from design to manufacture, Adv. Mater. Res. 633 (2013) 135–147, https://doi.org/10.4028/www.scientific.net/AMR.633.135.

[9] M.V. Ribeiro, M.R.V. Moreira, J.R. Ferreira, Optimization of titanium alloy (6Al-4V) machining, J. Mater. Process. Technol. 143–144 (2003) 458–463, https://doi.org/10.1016/S0924-0136(03)00457-6.

[10] A. Khorasani, I. Gibson, M. Goldberg, G. Littlefair, On the role of different annealing heat treatments on mechanical properties and microstructure of selective laser melted and conventional wrought Ti-6Al-4V, Rapid Prototyp. J. 23 (2017) 295–304, https://doi.org/10.1108/RPJ-02-2016-0022.

[11] C. Qiu, N.J.E. Adkins, M.M. Attallah, Microstructure and tensile properties of selectively laser-melted and of HIPed laser-melted Ti–6Al–4V, Mater. Sci. Eng. A 578 (2013) 230–239, https://doi.org/10.1016/j.msea.2013.04.099.

[12] W. Xu, S. Sun, J. Elambasseril, Q. Liu, M. Brandt, M. Qian, Ti-6Al-4V additively manufactured by selective laser melting with superior mechanical properties, Jom 67 (2015) 668–673, https://doi.org/10.1007/s11837-015-1297-8.

[13] H. Attar, M. Calin, L.C. Zhang, S. Scudino, J. Eckert, Manufacture by selective laser melting and mechanical behavior of commercially pure titanium, Mater. Sci. Eng. A 593 (2014) 170–177, https://doi.org/10.1016/j.msea.2013.11.038.

[14] S. Cao, R. Chu, X. Zhou, K. Yang, Q. Jia, C.V.S. Lim, A. Huang, X. Wu, Role of martensite decomposition in tensile properties of selective laser melted Ti-6Al-4V, J. Alloy. Compd. (2018), https://doi.org/10.1016/j.jallcom.2018.02.111.

[15] A.E. Wilson-Heid, Z. Wang, B. McCornac, A.M. Beese, Quantitative relationship between anisotropic strain to failure and grain morphology in additively manufactured Ti-6Al-4V, Mater. Sci. Eng. A 706 (2017) 287–294, https://doi.org/10.1016/j.msea.2017.09.017.

[16] H.K. Rafi, N.V. Karthik, H. Gong, T.L. Starr, B.E. Stucker, Microstructures and mechanical properties of Ti6Al4V parts fabricated by selective laser melting and electron beam melting, J. Mater. Eng. Perform. 22 (2013) 3872–3883, https://doi.org/10.1007/s11665-013-0658-0.

[17] A. du Plessis, S.G. le Roux, G. Booysen, J. Els, Directionality of cavities and porosity formation in powder-bed laser additive manufacturing of metal components investigated using X-Ray tomography, 3D print, Addit. Manuf. 3 (2016) 48–55, https://doi.org/10.1089/3dp.2015.0034.

[18] M. Tang, P.C. Pistorius, J.L. Beuth, Prediction of lack-of-fusion porosity for powder bed fusion, Addit. Manuf. 14 (2017) 39–48, https://doi.org/10.1016/j.addma.2016.12.001.

[19] T. Vilaro, C. Colin, J.D. Bartout, As-fabricated and heat-treated microstructures of

the Ti-6Al-4V alloy processed by selective laser melting, Metall. Mater. Trans. A 42 (2011) 3190–3199, https://doi.org/10.1007/s11661-011-0731-y.
[20] M. Peters, J. Hemptenmacher, J. Kumpfert, C. Leyens, Structure and properties of titanium and titanium alloys, in: Titan. Titan. Alloy. Fundam. Appl., Wiley-VCH Verlag GmbH & Co. KGaA, Weinheim, FRG, 2005: pp. 1–36. ⟨http://dx.doi.org/10.1002/3527602119.ch1⟩.
[21] D. Mohr, M. Dunand, K.H. Kim, Evaluation of associated and non-associated quadratic plasticity models for advanced high strength steel sheets under multi-axial loading, Int. J. Plast. 26 (2010) 939–956, https://doi.org/10.1016/j.ijplas.2009.11.006.
[22] X. Gao, T. Zhang, J. Zhou, S.M. Graham, M. Hayden, C. Roe, On stress-state dependent plasticity modeling: significance of the hydrostatic stress, the third invariant of stress deviator and the non-associated flow rule, Int. J. Plast. 27 (2011) 217–231, https://doi.org/10.1016/j.ijplas.2010.05.004.
[23] Y. Bai, T. Wierzbicki, A new model of metal plasticity and fracture with pressure and Lode dependence, Int. J. Plast. 24 (2008) 1071–1096, https://doi.org/10.1016/j.ijplas.2007.09.004.
[24] Y. Bai, T. Wierzbicki, Application of extended Mohr-Coulomb criterion to ductile fracture, Int. J. Fract. 161 (2010) 1–20, https://doi.org/10.1007/s10704-009-9422-8.
[25] V. Tuninetti, G. Gilles, O. Milis, T. Pardoen, A.M. Habraken, Anisotropy and tension-compression asymmetry modeling of the room temperature plastic response of Ti-6Al-4V, Int. J. Plast. 67 (2015) 53–68, https://doi.org/10.1016/j.ijplas.2014.10.003.
[26] O. Cazacu, B. Plunkett, F. Barlat, Orthotropic yield criterion for hexagonal closed packed metals, Int. J. Plast. 22 (2006) 1171–1194, https://doi.org/10.1016/j.ijplas.2005.06.001.
[27] J.T. Hammer, R.S. Yatnalkar, J.D. Seidt, A. Gilat, Plastic Deformation of Ti-6Al-4V Plate over a Wide Range of Loading Conditions, in: Dyn. Behav. Mater. Vol. 1 Proceedings 2012 Annu. Conf. Exp. Appl. Mech., 2013, pp. 165–169. ⟨http://dx.doi.org/10.1007/978-1-4614-4238-7⟩.
[28] J.T. Hammer, Plastic Deformation and Ductile Fracture of Ti-6Al-4V under Various Loading Conditions, The Ohio State University, 2012. ⟨http://rave.ohiolink.edu/etdc/view?acc_num=osu1354700435⟩.
[29] M.B. Gorji, T. Tancogne-Dejean, D. Mohr, Heterogeneous random medium plasticity and fracture model of additively-manufactured Ti-6Al-4V, Acta Mater. 148 (2018) 442–455, https://doi.org/10.1016/j.actamat.2018.02.025.
[30] ASTM International, Standard Specification for Wrought Titanium-6Aluminum-4Vanadium Alloy for Surgical Implant Applications (UNS R56400) 1, 2015. ⟨http://dx.doi.org/10.1520/F1472-14.2⟩.
[31] ASTM International, F2924: Standard Specification for Additive Manufacturing Titanium-6 Aluminum-4 Vanadium with Powder Bed Fusion, 2014. ⟨http://dx.doi.org/10.1520/F2924-12A.2⟩.
[32] ASTM International, Standard Test Methods for Tension Testing of Metallic Materials, 2016. ⟨http://dx.doi.org/10.1520/E0008⟩.
[33] D. Mohr, M. Oswald, A new experimental technique for the multi-axial testing of advanced high strength steel sheets, Exp. Mech. 48 (2008) 65–77, https://doi.org/10.1007/s11340-007-9053-9.
[34] P. Reu, Virtual strain gage size study, Exp. Tech. 39 (2015) 1–3, https://doi.org/10.1111/ext.12172.
[35] S. Palanivel, A.K. Dutt, E.J. Faierson, R.S. Mishra, Spatially dependent properties in a laser additive manufactured Ti–6Al–4V component, Mater. Sci. Eng. A 654 (2016) 39–52, https://doi.org/10.1016/j.msea.2015.12.021.
[36] R. Hill, A theory of the yielding and plastic flow of anisotropic metals, Proc. R. Soc. A Math. Phys. Eng. Sci. 193 (1948) 281–297, https://doi.org/10.1098/rspa.1948.0045.
[37] Simulia, Abaqus User Manual v2016; 2016. ⟨https://www.3ds.com/products-services/simulia/⟩.
[38] B. Carroll, T.A. Palmer, A.M. Beese, Anisotropic tensile behavior of Ti–6Al–4V components fabricated with directed energy deposition additive manufacturing, Acta Materialia 87 (2015) 309–320, https://doi.org/10.1016/j.actamat.2014.12.054.